Metal-free design of a multilayered metamaterial with chirped Bragg grating for enhanced radiative cooling

D. OSUNA RUIZ,[1,*] ![ORCID] C. LEZAUN,[1] A. E. TORRES-GARCÍA,[1] AND M. BERUETE[1,2,3] ![ORCID]

[1]*Department of Electrical, Electronic and Communications Engineering, Public University of Navarra, 31006 Pamplona, Spain*
[2]*Institute of Smart Cities (ISC), 31006 Pamplona, Spain*
[3]*miguel.beruete@unavarra.es*
[*]*david.osuna@unavarra.es*

Abstract: A wideband, all-dielectric metamaterial structure for enhancing radiative cooling is investigated. The structure is optimized to reflect most of the solar irradiance window (between 0.3 μm–3 μm), which is one of the biggest challenges in highly efficient radiative cooling coatings. The design is based on the principles of Bragg gratings, which constitutes a simple synthesis procedure to make a broadband reflector of reduced dimensions, without metallic layers, while keeping a flat enough response in the entire bandwidth. Numerical results show that reflection of solar irradiation can be easily tailored and maximized using this method, as well as the net cooling power of the device, about ~79 W/m^2 at daytime (about double at night-time) and a temperature reduction of 23 K (assuming no heat exchange) and 7 K assuming a heat exchange coefficient of 10 W/m^2/K, for a device and ambient temperatures of 300 K and 303 K, respectively. This occurs even in detriment of absorption in the atmospheric window (8 μm–13 μm). Results also show the importance of efficiently reflecting solar irradiance for such technologies and its relevance in synthesis and design without using metallic components.

1. Introduction

Radiative cooling (RC) is a natural phenomenon that allows for the passive cooling of an object by taking advantage of heat loss via radiation [1,2]. A positive net cooling power (P_n) occurs thanks to a combination of factors. The peak of black body radiation at ambient temperature ($T_{amb} \sim 300$ K) occurs within the atmospheric window (AW), a band ranging from 8 μm to 13 μm, in which the atmosphere is transparent. This feature enables efficient cooling of the object through direct radiation to outer space. Nevertheless, solar irradiance (I) is a significant source of heating, given its high power density between 0.3 μm and 3 μm [3]. Hence, to maximize P_n in daytime RC devices, it is highly desirable to minimize the influence of I, especially given its variability when accounting for day-night cycles, weather changes, or different climatic regions. The latter would also help to generalize the use of such technologies, making them less dependent on time and place of use. Photovoltaic technology also benefits from daytime RC, as the efficiency and lifetime of systems worsen with increasing temperatures [4,5].

At thermal equilibrium, the emissivity of an object is equal to its absorbance (A), as follows from Kirchoff's theorem [1]. Therefore, an ideal RC device should have simultaneously a high reflectance (R) in the solar spectrum and a high A in the AW. To fulfill these constraints, multilayered (ML) thin film structures composed of stacked materials with high index contrast have been proposed, such as TiO_2/SiO_2 or HfO_2/SiO_2 backed with a metallic reflector like Ag or Al [6–9]. TiO_2 is widely used for RC coatings due to its high R in the visible region and its advantages when deposited on SiO_2, such as chemical stability and corrosion and stress reduction

[10]. Following this strategy, Yao *et al.* [11] proposed a multilayer (ML) thin film structure that enhances both solar reflection and AW emission. However, the ML synthesis was complex and expensive due to the use of multiple materials. Raman *et al.* [8] used HfO_2 instead of TiO_2 for an improved absorbing performance, but the toxicity of HfO_2 appears as a clear practical disadvantage of such design. The use of nanocavities and other absorbers, such as Si_3N_4, can not only improve P_n, but also enhance the aesthetics of the coatings by emitting visible color wavelengths [12]. In addition, other techniques such as topping the ML with gratings and/or metasurfaces (MTSs) [5,13] have been proposed, including those based on natural radiators or biomimetic MTSs [14]. All these approaches aim to improve R at the layer interfaces, A in the bulk, or both simultaneously [8]. However, a common issue is the high losses of the metallic layers in the solar window which increase solar A reducing P_n. Therefore, designing an all-dielectric ML can be a more optimal approach.

The Transfer Matrix Method and coupled-mode theory can be used to analyze the reflectance spectrum of MLs [7,15]. Synthesis methods based on the Discrete Layer Peeling (DLP) algorithm [16,17] have been proposed for designing ML thin film structures. However, the complexity of synthesis methods increases exponentially with the number of layers and materials, making it impractical for large-scale applications. As previously shown in the literature review, such complex MLs are typically required for RC. To overcome this limitation, alternative approaches such as genetic or surrogate algorithms and artificial intelligence methods have been developed to determine the optimal structural parameters, including layer thicknesses and locations within the ML [8,18].

Therefore, a fully analytical method for designing a broadband reflective ML with simpler synthesis is highly desirable for RC. In this regard, one can think of fiber Bragg gratings (FBGs) which have been extensively used as key components for selective frequency rejection in telecommunication networks due to their simple working principle, which is based on Fresnel reflections. They create high n-contrast mirrors by spatially modulating the index of refraction (n) periodically distributed along the 1-D grating. Chirped FBGs (CFBGs) introduce a gradual variation of the index (periodicity is not constant) and are typically used to correct chromatic dispersion and widen the reflected bandwidth (BW) in a small percentage, but at the cost of increasing length and complexity [19]. When it comes to the synthesis of CFBGs from a target reflectance spectrum, it can become complex and physical parameters are typically retrieved after full numerical inverse synthesis methods [18,20,21]. For instance, Quintela *et al.* [18] proposed an adaptive algorithm that adds sub-FBGs to achieve an arbitrary target spectrum.

Hence, in the context of RC the key question is: can the solar window be efficiently reflected with a simpler, thinner ML based on the chirped Bragg gratings (CBGs) design principles? In that sense, previous works have shown broadband R by modifying porosity of TiO_2 layers for a certain polarisation [22,23], pyramidal growth for the layers [24] or by topping the ML with photonic crystals [13]. However, these methods are still sub-optimal due to their design and fabrication complexity. Despite their clear advantages, TiO_2 or HfO_2 on SiO_2 are not suitable materials for making simpler designs due to their high material cost and even toxicity [8]. A solar reflector based on an ML Bragg grating should also be entirely functional without backing metallic layers and work for multiple polarisations of light. To the best of our knowledge, such an optimal candidate remains elusive and has not been identified yet.

Here we explore the synthesis of a chirped metamaterial for RC applications using CBGs design criteria, dedicated to maximise and optimise R in an all-dielectric ML. While metals always show strong absorption at such frequencies [11], the use of only dielectric materials allows to control reflection in the solar window and tailor the reflected BW. Chirped MLs have been explored mostly for enhancing wave matching, absorption and/or pulse shaping, in acoustics [25], electromagnetics [26], up to extremely high frequencies (X-rays) [21]. On the contrary, and since I is a source of major heating [8,27], our goal here is rather to maximise P_n by reflecting the

most in the solar window. Therefore, while the relation between P_n, the reflected BW and the total ML thickness (t_{ML}) is generally not obvious, a large P_n along with a low t_{ML} is the optimal combination for practical use. In what follows, we present different results in two scenarios. Firstly, exploring the role of the number of sections (N) in the grating for a fixed BW and secondly, fixing N and varying the BW. In particular, we will aim to infer and isolate the relevance of I in the ML design. This work will be practical for designing more compact and efficient Bragg-based devices for RC. The main conclusions are summarised after the thorough numerical study.

2. Materials and methods

Figure 1(a) shows a schematic of a CBG-inspired ML geometry model with $N = 6$ sections (12 layers). A section is defined as two bottom-up stacked layers of materials in a 'low-index'/'high-index' fashion. Rather than the commonly used SiO_2 and TiO_2 layers in ML structures, we investigated the advantages of using materials with higher index contrast for an enhanced R in the solar window. For instance, such combination of materials might be SiO_2 and Si in order to further broaden the reflected BW, as they have a greater index contrast than that of SiO_2 and TiO_2 while still show global absorption in the AW [see Supplement 1]. Besides, the manufacturing process of SiO_2/Si multilayered structures as Bragg reflectors is well known [28]. A more detailed discussion on the choice of the material models for simulations, also regarding fabrication of a ML with such materials, is provided in Supplement 1. The latter information is supplementary for the aim of the present work, but becomes very relevant regarding manufacturing and fabricating of an experimental prototype, which is envisioned as future work. To simplify the notation, we will use subscripts $i = 1$ and $i = 2$ to refer to the 'low index' (n_1) and 'high index' (n_2) materials, respectively, throughout the rest of this article. As shown in Fig. 1, the structure is supported by a SiO_2 substrate slab that has a thickness of 0.5 mm. The substrate is a lossy material and it is always electrically very large (always between $\sim$ 17 and $\sim$ 1785 times the working wavelength) in the entire range of the explored λ (between 0.28 µm and 30 µm). Thus, this thickness ensures that we can safely assume that practically no power is transmitted beyond the substrate, leading to a negligible transmission ($T \ll R$) and thus $A = 1 - R$.
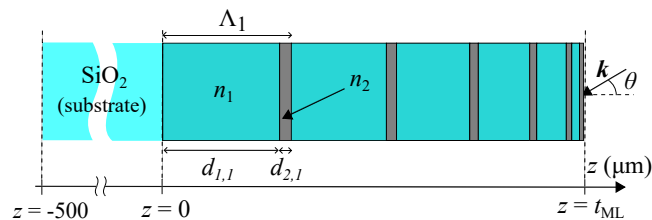

Fig. 1. (a) Schematic showing an exemplary ML structure of thickness t_{ML} grown along the z direction and infinite in the $x - y$ plane. The view perspective is rotated 90 degrees for convenience. Layers of the low index (n_1) and high index (n_2) materials are shown in blue and grey, respectively. The layer thicknesses ($d_{i,1}$) and 'period' (Λ_1) of the first (left-most) section in the chirp are indicated. An impinging wave with incident angle θ from the air above (right-most region) is indicated by its wavenumber vector $\boldsymbol{k}$.

We employed GD-Calc, an open-source, MATLAB-based numerical software that utilizes a generalized variant of the rigorous coupled-wave (RCW) diffraction theory [29], to study an equivalent model of uniform cross-section in the x and y directions [30]. To increase the reflection of the incident wave from the top surface (a TE or TM mode with incident angle θ), a layer of the high refractive index material is placed as the topmost layer of the ML structure, creating a significant mismatch between the refractive indices of air and the ML. We conducted calculations and simulations for several incidence angles ranging from 0 to 80 degrees in steps

of 10 degrees. Given the nature of the solar source, the impinging wave with a wavenumber of $k = 2\pi/\lambda$ was assumed to be non-polarized, so that it had both orthogonal components of the electric field. Using GD-Calc, we obtained the average reflectance $R(\lambda, \theta)$ from both TE and TM modes as a function of wavelength (λ) and incidence angle (θ). The reader is referred to Supplement 1 simulation results that show the dependence of the averaged R (A) with increasing θ, in accordance with Fresnel equations in a ML structure and other complementary studies such as calculations based on coupled-mode theory [15] leading to identical results. Using the calculated absorbance $A(\lambda, \theta)$, which, as previously mentioned, is equivalent to emissivity in thermal equilibrium, we computed the radiated power (P_{rad}), atmospheric power (P_{atm}), and Sun power (P_{sun}). Finally, P_n was obtained as $P_n = P_{rad} - P_{sun} - P_{atm}$, assuming an ambient and device temperature of $T_{amb} = 303$ K and $T_d = 300$ K, respectively, for sub-ambient RC [9,31]. A more detailed mathematical description for each power calculation can be found elsewhere [1]. Initially, a non-radiative heat transfer coefficient equal to zero ($h_c = 0$ W/m^2/K) is assumed. Equivalently, no thermal losses are incorporated into the models [32]. The latter is even more true for an all-dielectric structure, which is precisely our case, than for one including metals.

For the CBG designs examined in this paper, we devised a 'chirping' function $\Lambda(z)$ to achieve the flattest possible reflection BW between λ_1 and λ_N, where λ_k represents the 'targeted' reflected Bragg wavelength of section number k ($1 \leq k \leq N$). While it is essential to minimize the number of sections (N) to reduce the thickness of the ML structure, having a very small N may result in a degraded, less flat reflected BW, even with high index contrast materials [19]. Therefore, there is a trade-off between the accuracy of the targeted reflection curve (which is improved with a higher N) and the thickness of the structure (which increases with N). A linearly chirped step function can be defined as $\Lambda_L(z) = \Lambda_1 + Cz$, where Λ_1 is the thickness (or period if the section was repeated) of the bottom-most section, and $\pm C$ determines the direction and magnitude of the chirping effect. The direction of the chirping (positive or negative) primarily influences the dispersion compensation and pulse shaping properties of the ML structure [19,21] and not necessarily reflected power, specially if materials are lossless. Supplementary analysis of a positive chirp shows that the performance of the chirped ML in the solar window is practically unaltered if $C>0$. For convenience, we use a bottom-up decreasing chirp ($C<0$).

The thicknesses of the bottom-most and top-most sections ($k = 1$ and $k = N$, respectively) were determined by satisfying the Bragg wavelength condition $\lambda_k = 2n_{eff,k}(d_{1,k} + d_{2,k})$, where $d_{1,k}$ and $d_{2,k}$ are the thicknesses of each material for section k, and $n_{eff,k} = (n_{1,k}d_{1,k} + n_{2,k}d_{2,k})/(d_{1,k} + d_{2,k})$ is the effective refractive index for section k, where $n_{i,k} = n_i(\lambda_k)$ accounting for dispersion. To ensure that the structure can be fabricated, the minimum thickness layer (i.e., that of material $i = 2$ and section $k = N$) was set to $d_{2,N} = 0.02$ μm. The thickness of the 'low-index' material thinnest layer, $d_{1,N}$, has to be determined 'ad-hoc' clearing it from the Bragg condition for $\lambda_N = 0.3$ μm. Besides, if the materials show almost no dispersion, the rest of layer *physical thicknesses* ($d_{i,k}$) can be linearly increased, from the top to the bottom of the ML until the Bragg condition for λ_1 is satisfied. If materials show significant dispersion, $d_{i,k}$ can still be retrieved as long as the Bragg condition is fulfilled for the *effective optical thicknesses*. A more detailed description of the algorithm can be found in Supplement 1. The total thickness of the ML is $t_{ML} = \sum_{k=1}^{N} d_{1,k} + d_{2,k}$.

3. Numerical studies

For the next studies, we used the optical properties from exemplary models of SiO$_2$ and Si, given their high index contrast and absorption of SiO$_2$ in the AW. Nevertheless, other material models might be used as well.

3.1. Influence of the number of layers for a fixed bandwidth

In this study, the BW limits were fixed to approximately half of the solar window ($\lambda_N = 0.3$ μm and $\lambda_1 = 2.1$ μm), where 96.7% of I is contained, calculated via numerical methods. The number

of sections (N) was varied from 3 to 30 in steps of 3. Figure 2(a) illustrates how the reflected BW flattens as N increases for a normally incident wave ($\theta = 0°$) for three selected cases: $N = 3$ (blue circles), $N = 9$ (green '×') and $N = 30$ (yellow crosses). R curves at other θ are shown in the Supplement 1. The theoretically calculated Bragg wavelengths, λ_N and λ_1, match the limits of the simulated reflected BW very well, as shown by the vertical dashed lines. In CFBGs, when the number of sections N is low, the performance of the Bragg grating deteriorates because the grating step is too large to cover the relatively wide BW, therefore the global contribution of Fresnel reflections (also weaker due to the small index contrast) reduces and the BW becomes less flat [19]. The required N in CFBGs is typically high, normally in the order of hundreds [19]. Note that, in our MLs designs, as N reduces, so does its performance, similarly to CFBGs. On the other hand, a reasonably good performance and flat reflected BW is achieved with considerably smaller values of N. This can be partially explained by the greater contrast of indices between layers in the ML. Figure 2(b-c) illustrates the variation of P_n and t_{ML} as a function of N. The increase in N leads to a clear enhancement of P_n, which can be modelled by an exponential function with parameters a and b: $P_n(N) = P_{n,max}(1 - e^{(-(N-a)/b)})$. As N approaches a critical value N_C, P_n approaches the asymptotic value of $P_{n,max} \approx 72$ W/m^2 of the fit and the increment in P_n becomes negligible (when 90% of the asymptotic value is reached). Naturally, t_{ML} linearly increases with N (see Fig. 2(c)).
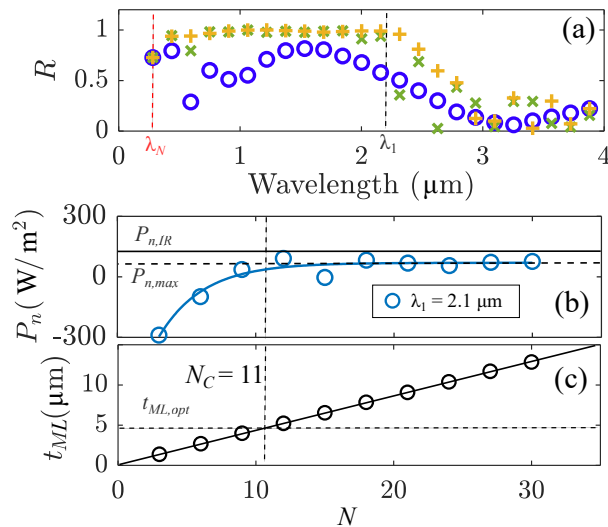

Fig. 2. (a) Simulated reflectance ($R(\lambda, 0)$) for $N = 3$ (blue circles), $N = 9$ (green '×') and $N = 30$ (yellow crosses) for a fixed BW ($\lambda_1 = 2.1$ µm). Vertical dashed lines are the theoretically calculated Bragg wavelengths for the shortest (λ_N) and longest (λ_1) sections in the ML. (b) Calculated P_n (open circles) from the simulated $A(\lambda, \theta)$ and a fit to the exponential (solid line). Horizontal dashed line is the asymptotic value of the fit and solid line is net power for an ideal radiator. (c) Total thickness of the ML (t_{ML}) as a function of N. Vertical dashed line indicates the optimal number of sections N_C for $\lambda_1 = 2.1$ µm.

In order to evaluate results quantitatively, we obtained the optimal P_n that an ideal radiator (IR) would provide under the same environmental (Sun irradiance and atmospheric emission) and temperature conditions as for the chirped ML designs. Such $P_{n,IR}$ can be calculated from an ideal R curve at $T_{amb} = 303$ K which, from Ref. [33], is defined piecewise as $R_{IR}(\lambda) = 0$ if $\lambda \leq 4$ µm and $R_{IR}(\lambda) = 1$ if $\lambda > 4$ µm, at the same ambient and device temperatures, and assuming a cosine decay with increasing θ [34]. We obtain $P_{n,IR} = 140$ W/m^2 (see solid line in Fig. 2(b)), therefore the asymptotic $P_{n,max}$ provided by the fit to our results is about 51% of that of an IR.

We also acknowledge that, in a real sub-ambient RC scenario, heat losses will reduce P_n [1,32]. However, $P_n > 0$ is still expected given the typically low losses (1 W/m^2/K < h_c < 10 W/m^2/K) [1,24,35] under sub-ambient conditions and the given temperature difference ($T_{amb} - T_d = 3$ K). The latter is further explored in section 3.4.

Besides, results suggest a practical lower limit for N to achieve a flat-enough BW, maximum P_n, and minimum t_{ML}. Using the exponential model, such value N_C can be approximated as the value of N at which P_n, as a function of N, either reaches 90% of $P_{n,max}$ (i.e., 64.8 W/m^2) or exceeds it for the first time since, in practice, the asymptotic value would have been reached. For $N = 11$, $P_n = 66.8$ W/m^2, and this way, we find $N_C = 11$.

For $N = 11$, the minimum value of t_{ML} is found to be ~ 5 µm, as shown in Fig. 2(c). To put our results into context, it is worth noting that in Ref. [13], an MgF$_2$/TiO$_2$/SiC/SiO$_2$ ML of 12.3 µm is also proposed. In Ref. [36], an SiO$_2$/TiO$_2$/Al$_2$O$_3$ ML of 1.9 µm and in Ref. [37], a polymer-based ML of 67 µm are proposed. Only the ML from Ref. [36] was thinner than our proposal, but in all the previous works a backing metallic (Ag) layer is still required as well as a combination of more than two materials. These aspects are not desirable in environmental terms.

Therefore, it is possible to achieve optimal P_n and t_{ML} without the need to increase N indefinitely in the chirped grating. Indeed, from the obtained results it is clear that increasing the number of sections, N, smooths the chirping step but over-flattens the reflected BW and unnecessarily thickens the structure, which can complicate fabrication. This is because the added sections linearly increase in thickness as more λ_k are targeted. Since neither R nor P_n are significantly improved with increasing N, an optimal value of $N_C = 11$ can be chosen. Under this condition, P_n is maximized while t_{ML} is minimized, resulting in an optimal design of our ML.

3.2. Influence of the bandwidth for a fixed number of layers

In this second study, N is fixed to 24 and the top limit (λ_1) of the reflected BW is varied from 0.35 µm to 3.35 µm in steps of 0.25 µm. A large N is chosen to ensure that no errors are present due to a malfunctioning Bragg grating (see previous section). Figure 3(a) shows the simulated R spectrum for three values of λ_1: 1.1 µm (blue circles), 2.1 µm (green '×') and 3.1 µm (yellow crosses), at $\theta = 0\circ$. Similarly to the previous section, the theoretically predicted boundaries λ_N and λ_1 are in excellent agreement with the simulated reflected BW for each case, as indicated by the vertical dashed lines.

Figure 3(b-d) illustrates the variation of the calculated P_n, its rate of change as λ_1 increases, $(P_n(\lambda_1^{i+1}) - P_n(\lambda_1^i))$, referred to as ΔP_n for convenience), and t_{ML} as a function of λ_1. As anticipated, the increase in λ_1 (i.e., broadening BW) leads to an increase in P_n. Again, P_n can be fitted to the following function: $P_n(\lambda_1) = P_{n,max}(1 - e^{(-(\lambda_1-a)/b)})$. From the fit, a maximum value of P_n is achieved at a critical value $\lambda_{1,C}$ beyond which ΔP_n approaches zero (when 90% of the asymptotic P_n value is reached). This behavior can be attributed to the shape of the $I(\lambda)$ curve (depicted as the orange curve in Fig. 3(c)), which matches qualitatively well with the values of ΔP_n, as it will be explained in detail in the next study. Solving for $\lambda_{1,C}$ in $P_n(\lambda_{1,C}) = 0.9P_{n,max}$ yields $\lambda_{1,C} = 2.0$ µm. The asymptotic maximum P_n obtained from the fit is $P_{n,max} \approx 79$ W/m^2 (54% of $P_{n,IR}$), about as large of that from the previous study. Figure 3(d) illustrates that, similar to the previous case, t_{ML} also increases linearly with λ_1. This is because the additional new sections contribute to a linearly chirped grating. However, adding thicker layers to improve R above $\lambda_{1,C}$ would be pointless, as P_n does not increase significantly, while t_{ML} continues to increase indefinitely. This once again demonstrates that a minimal and optimal t_{ML} can be obtained. For $N = 24$, a linear fit yields $t_{ML,opt} \approx 6$ µm, for $\lambda_{1,C} = 2.0$ µm. This is reasonable because the intensity of $I(\lambda)$ significantly decreases beyond ~ 2 µm, leading to a strong correlation with ΔP_n. Remarkably, there is good resemblance between ΔP_n and I even despite the fact that we only considered optimisation of solar reflection in our designs while P_n clearly depends on other environmental factors too. It is well known that P_{sun} strongly affects P_n [5,8], making solar I a first-order effect.
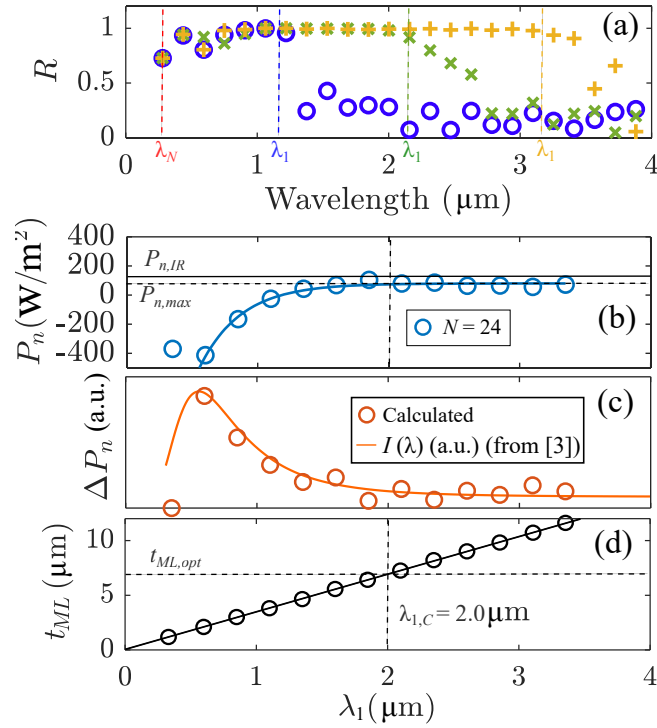
Fig. 3. (a) Simulated reflectance ($R(\lambda, 0)$) for λ_1 = 1.1 µm (blue circles), λ_1 = 2.1 µm (green '×') and λ_1 = 3.1 µm (yellow crosses) for a fixed number of sections (N = 24). Vertical dashed lines are the theoretically calculated Bragg wavelengths for the shortest (λ_N) and longest sections in the ML (for each λ_1). (b) Calculated P_n (open circles) from the simulated $A(\lambda, \theta)$ and a fit to the exponential (blue solid curve). Horizontal dashed line is the asymptotic value of the fit and black solid line is net power for an ideal radiator. (c) Rate of change of P_n ($\Delta P_n = P_n(\lambda_1^{i+1}) - P_n(\lambda_1^i)$) overlaid to the irradiance curve of the Sun, (from [3]) in arbitrary units. (d) Total thickness of the ML as a function of λ_1. Vertical dashed line indicates the optimal upper limit of the reflected BW ($\lambda_{1,C}$) for N = 24.

As novelty, we show that this influence can be quantified by ΔP_n. This is one of our key results, which allows to quantify to a degree the greater influence of I on the cooling performance. In the following study, we further explore whether the qualitative resemblance between $I(\lambda)$ and ΔP_n is consistent within the models used and thus, dominant with respect to other factors such as atmospheric losses. This will allow to optimise the ML synthesis process regarding solar reflection, with $I(\lambda)$ becoming the 'target curve' in the design process.

3.3. Influence of solar irradiance

In the previous studies, irradiance I is obtained from the model provided in Ref. [3]. To check the consistency of ΔP_n with such magnitude, one can perform the same comparative with a different I curve, and check if the trend following the new ΔP_n is similar as well. Figure 4 shows results where the solar I is replaced by a model of a normalised I from α−Centauri ($I_{\alpha-C}$), with a black-body temperature of 3042 K (see Refs. [38,39]), on atop the putatively weak or even non-existent atmosphere (see Ref. [40]) of Proxima b, its orbiting planet [39] and thus $P_{atm} \sim 0$. To qualitatively compare with solar I, they are both normalised to their respective maxima. The step size in λ_1 between simulations is 0.25 µm. The overall resemblance between I and ΔP_n in

both cases is clear. These results also suggest similar trends for ΔP_n following any I if other environmental models were used instead. Therefore, it is possible to quantify the influence of I via the parameter ΔP_n or equivalently, obtaining several P_n as a function of λ_1.
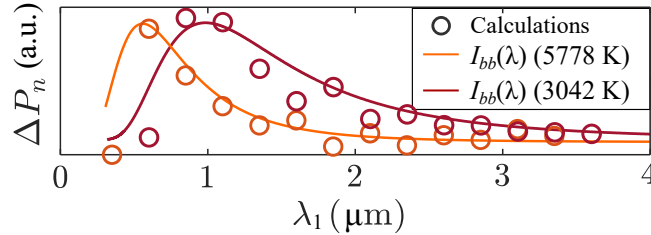

Fig. 4. Calculated ΔP_n for $T = 5778$ K (orange circles) and $T = 3042$ K (crimson circles) overlaid to the black body irradiance models for the Sun (orange) and α-Centauri (crimson) irradiance curves for the same temperatures, taken from [3] and [38], respectively. Results are in arbitrary units, normalised to their respective maxima for an easy comparison.

Following from the above, in the next study we present results using an adaptive (negative) 'chirping': The number of sections is adapted to solar $I(\lambda)$, putting more sections for those λ_k where I is greater ($n_k \propto I(\lambda_k)$). Further details on the discretisation process of I and the proportional distribution of sections per λ_k with increasing N are shown in Supplement 1. Figure 5(a) shows the simulated $R(\lambda, 0)$ for $N = 4$, $N = 11$ and $N = 34$. As N increases from 4 to 11, the matching of R to I improves, since more sections are dedicated to each λ_k. Noticeably, the distribution of sections for $N = 11$ (critical value from Section 3.1) resemble the most to I and also, it is the most similar to a linear chirp (i.e. one section per λ_k) while giving one more section to the three λ_k nearest to the maxima in I (~ 0.5 µm). The latter highlights the goodness of such type of chirp for the designed MLs. For larger N, the spectra appear clearly wider for larger λ_k than those in I with most intensity. This might be due to the intrinsic BWs for each individual λ_k, which become closer in frequency and may overlap as N increases (see Supplement 1 for an exemplary distribution of sections for $N>11$). This would suggest that a different criterion for the repetition of sections, instead of proportional to $I(\lambda_k)$, may compensate this effect. On the other hand, note that the linear chirping appears as the most equitable criterion regarding 'number of repetitions per λ_k'. A 'middle-ground' solution between both options, such as that obtained for $N = 11$ seems to be the optimal choice to get a reflectance curve that mimics $I(\lambda)$.

Our original goal was to demonstrate that our synthesis method, based on CBGs, allows to obtain a reflectance spectrum 'à-la-carte', that mimics any $I(\lambda)$ curve, given the sufficient number of sections in the Bragg grating (see Section 3.1). Indeed, our final (and optimised) results suggest so. Moreover, equivalent results were also obtained for positive chirps. Besides, this method is less computationally demanding than other numerical methods of synthesis [18].

One clear limitation may be the (sometimes) required high number of layers (equivalently N) and layer thicknesses, which may complicate the ML fabrication. Nonetheless, the proposed discretisation process leads in most cases to the elimination of long sections for large λ_k, as they render not meaningful given the profile of I. This also reduces the BW upper limit. In general, this leads to a reduction in P_n, but also a more pronounced reduction in t_{ML}. Figure 5(b-c) illustrate P_n, P_{sun} and t_{ML} as functions of N. Dashed line in Fig. 5(b) indicates the $P_{n,max}$ obtained from section 3.1. Naturally, P_n is strictly smaller than using a flat-top spectrum and is considerably reduced for low N given the expected malfunction of the Bragg grating [19]. For an 'adaptive chirping', while the dependence between variables is not trivial (as P_n is not monotonously increasing with N), it is clear that P_n is negatively correlated with P_{sun}. On the other hand, a linear fit still applies to t_{ML} with increasing N, but resulting into MLs thinner than those from section 3.1 (see dashed line, reproduced from Fig. 2(c)). For example, a total ML thickness of
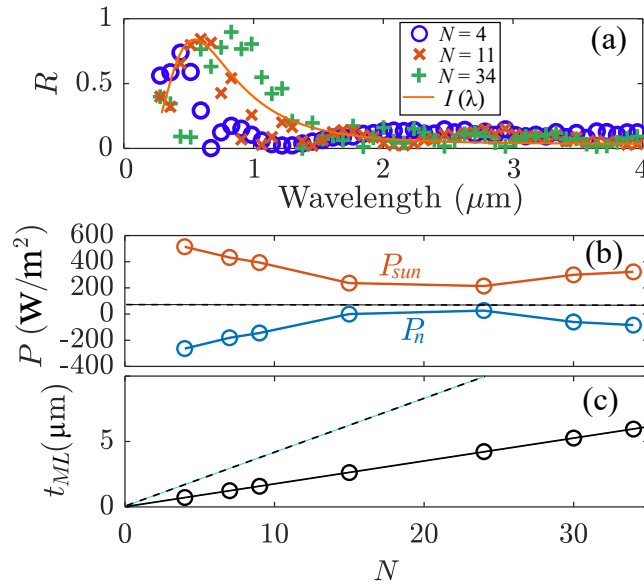
Fig. 5. Calculated R for $N = 4$ (blue circles), $N = 11$ (orange '×') and $N = 34$ (green crosses) overlaid to the irradiance curve of the Sun (orange curve) in arbitrary units for an easy comparison. (b) Calculated P_n and P_{sun}. Solid curves are for guiding the eye and they are not fitting curves. Dashed line indicates $P_{n,max} = 72$ W/m^2 obtained in section 3.1. (c) Total thickness of the ML as a function of N. Solid line is the linear fit to the data and dashed line is reproduced from Fig. 2(c).

approximately 1.5 μm is obtained with a chirp adapted to I, compared to 5 μm with a $N = 11$ linear chirp. For large enough N, replacing thicker sections by repeated thinner ones allows to reduce t_{ML} at the expense of a significant reduction in P_n. Given the reflectance curve from an ideal radiator [33], it seems that a linear chirp is an optimal choice for optimising P_n, while an adapted chirp is optimal for optimising t_{ML}. A combined optimisation of P_n and t_{ML} using a non-linear chirp is beyond the scope of this article, but it seems that a middle-ground solution is close to the optimal, but not trivial to find.

3.4. Equilibrium temperature and comparative study with other structures

So far in our work, P_n has been used as the only evaluation metric for the goodness of the proposed structure, and compared with that of an ideal radiator. In this section, we provide with an study on the equilibrium temperature (T_{eq}) of the optimal structure (for $N = 11$ and $\lambda_C = 2.0$ m) for $h_c = 0$ W/m^2/K, $h_c = 1$ W/m^2/K and $h_c = 10$ W/m^2/K. Also, a comparative study between the obtained P_n, T_{eq} to those of previous work on RC is shown.

Figure 6 shows P_n as a function of $T_d − T_{amb}$ (with T_d ranging from 200 K to 320 K) and h_c. The T_{eq} is achieved when $P_n = 0$ (see horizontal dashed line), and it is clearly reduced as h_c increases. A temperature reduction of about 23 K is obtained assuming no heat exchange and, even assuming the worst-case scenario for heat losses, a positive decrease of temperature of about 7 K is obtained (see vertical dashed lines).

Table 1 shows the obtained metrics for the worst realistic scenarios (largest h_c) reported in previous works on RC, during daytime. For our work, we assume $h_c = 10$ W/m^2/K for allowing us to compare a realistic worst-case scenario. We must stress that some of the results reproduced here correspond to experimental measurements and different device and/or ambient temperatures and atmospheric models [13]. Thus, a quantitative direct comparison with our results and other
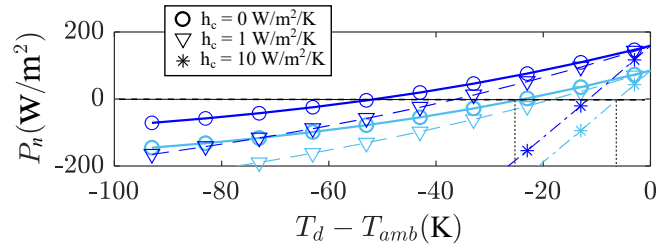
Fig. 6. Calculated P_n for $h_c = 0$ W/m^2/K (blue circles), $h_c = 1$ W/m^2/K (blue triangles) and $h_c = 10$ W/m^2/K (blue stars) for day-time scenarios (light blue curves) and night-time (dark blue curves), i.e. when $P_s = 0$. Vertical dashed lines show T_{eq} for the optimistic scenario (no losses) and pessimistic (maximum heat losses) scenario.

simulations is somewhat forced. Nonetheless, our proposed structure yields similarly large P_n, while stands out for being all-dielectric, not requiring patterned layers nor any metallic layer for achieving reflection, and also shows a considerable small thickness and great temperature reduction.

Table 1. Comparison of standard evaluation metrics between the results obtained and other previous works on day-time radiative cooling, for a worst-case (high losses) scenario.

Ref.	P_n (W/m^2)	T_{eq} (K)	Metallic layers	Patterned layers
[8]	40.1	278	yes (Ag)	no
[24]	156	283	no	yes
[35]	77.5	8.3	yes (Ag)	yes
[13]	70	296	yes (Ag)	yes
[11]	46	284	yes (Ag)	no
Our work	79	7	no	no

4. Conclusion

To conclude, we have demonstrated the feasibility of making highly efficient, compact ML reflective structures for sub-ambient RC, where the novelty is the application of chirped Bragg grating principles using only two, high contrast index materials, mostly lossless, without a backing metallic layer. Numerical results show a maximisation of P_n when the efforts are focused on reflecting I mostly, even above optimising emissivity in the AW (extended results up to 26 μm can be found in Supplement 1). Using a linear chirp, the optimal P_n and t_{ML} obtained are $\sim$ 79 W/m^2 at daytime ($\sim$ 54% of an ideal radiator under the same temperature conditions) and $\sim$ 5 μm, respectively, with reasonable environmental models and an ambient (device) temperature of 303 K (300 K). A positive net cooling power and a decrease in temperature (7 K) is still obtained even considering a worst-case scenario for heat losses, modelled by a heat exchange coefficient of $h_c = 10$ W/m^2/K.

We acknowledge that results can be drastically different depending on the environmental models employed. In fact, P_n is partially calculated from such models, which to some extent explains the good fit to $I(\lambda)$ in Fig. 3(c) and Fig. 4. However, we showed that the qualitative resemblance between $I(\lambda)$ and P_n is consistent within the models used and thus, irradiance is dominant with respect to other factors such as atmospheric losses, suggesting a similar trend if

other models were used instead (see Fig. 4). RC and photovoltaic devices, among other cooling coating technologies, could benefit from these insights.

Disclosures. The authors declare no conflicts of interest.

Data availability. Data underlying the results presented in this paper are not publicly available at this time but may be obtained from the authors upon reasonable request.

Supplemental document. See Supplement 1 for supporting content.

References

1. B. Zhao, M. Hu, X. Ao, N. Chen, and G. Pei, "Radiative cooling: A review of fundamentals, materials, applications, and prospects," Appl. Energy **236**, 489–513 (2019).
2. Z. Chen, L. Zhu, A. Raman, and S. Fan, "Radiative cooling to deep sub-freezing temperatures through a 24-h day–night cycle," Nat. Commun. **7**(1), 13729 (2016).
3. "Nrel, solar irradiance spectra," http://www.nrel.gov/grid/solar-resource/spectra-am1.5.html.
4. Z. Wang, D. Kortge, J. Zhu, Z. Zhou, H. Torsina, C. Lee, and P. Bermel, "Lightweight, passive radiative cooling to enhance concentrating photovoltaics," Joule **4**(12), 2702–2717 (2020).
5. G. Perrakis, A. Tasolamprou, G. Kenanakis, E. Economou, S. Tzortzakis, and M. Kafesaki, "Combined nano and micro structuring for enhanced radiative cooling and efficiency of photovoltaic cells," Sci. Rep. **11**(1), 11552 (2021).
6. R. S. Dubey and V. Ganesan, "Fabrication and characterization of TiO_2/SiO_2 based Bragg reflectors for light trapping applications," Results Phys. **7**, 2271–2276 (2017).
7. K. Han and J. H. Kim, "Reflectance modulation of transparent multilayer thin films for energy efficient window applications," Mater. Lett. **65**(15-16), 2466–2469 (2011).
8. A. Raman, M. Abou Anoma, L. Zhu, E. Rephaeli, and S. Fan, "Passive radiative cooling below ambient air temperature under direct sunlight," Nature **515**(7528), 540–544 (2014).
9. Y. Zhu, Y.-H. Ye, D. Wang, and Y. Cao, "Quasi-periodic selective multilayer emitter for sub-ambient daytime radiative cooling," AIP Adv. **11**(2), 025109 (2021).
10. R. Pessoa, W. Chiappim Junior, M. Fraga, and H. Maciel, "A historical overview of the research on TiO_2 thin films deposited by atomic layer deposition – part 1: Early studies".
11. K. Yao, H. Ma, M. Huang, H. Zhao, J. Zhao, Y. Li, D. Shuliang, and Y. Zhan, "Near-perfect selective photonic crystal emitter with nanoscale layers for daytime radiative cooling," ACS Appl. Nano Mater. **2**(9), 5512–5519 (2019).
12. S. Jin, M. Xiao, W. Zhang, B. Wang, B. Wang, and C. Zhao, "Daytime sub-ambient radiative cooling with vivid structural colors mediated by coupled nanocavities," ACS Appl. Mater. Interfaces **14**(49), 54676–54687 (2022).
13. E. Rephaeli, A. Raman, and S. Fan, "Ultrabroadband photonic structures to achieve high-performance daytime radiative cooling," Nano Lett. **13**(4), 1457–1461 (2013).
14. C. Campos-Fernández, D. E. Azofeifa, M. Hernández-Jiménez, A. Ruiz-Ruiz, and W. E. Vargas, "Visible light reflection spectra from cuticle layered materials," Opt. Mater. Express **1**(1), 85–100 (2011).
15. Z. M. Zhang and C. J. Fu, "Unusual photon tunneling in the presence of a layer with a negative refractive index," Appl. Phys. Lett. **80**(6), 1097–1099 (2002).
16. R. Feced, M. Zervas, and M. Muriel, "An efficient inverse scattering algorithm for the design of nonuniform fiber Bragg gratings," IEEE J. Quantum Electron. **35**(8), 1105–1115 (1999).
17. J. Skaar, L. Wang, and T. Erdogan, "On the synthesis of fiber bragg gratings by layer peeling," IEEE J. Quantum Electron. **37**(2), 165–173 (2001).
18. A. Quintela, J. M. Lazaro, M. A. Quintela, C. Jauregui, and J. M. Lopez-Higuera, "Fabrication of FBGs with an arbitrary spectrum," IEEE Sens. J. **8**(7), 1287–1291 (2008).
19. R. Kashyap, *Fiber bragg gratings 2nd edn*, (Academic Press, Burlington, 2009), chap. Chirped Fiber Bragg Gratings.
20. F. Lhommé, C. Caucheteur, K. Chah, M. Blondel, and P. Mégret, "Synthesis of fiber Bragg grating parameters from experimental reflectivity: a simplex approach and its application to the determination of temperature-dependent properties," Appl. Opt. **44**(4), 493–497 (2005).
21. A. Guggenmos, Y. Cui, S. Heinrich, and U. Kleineberg, "Attosecond pulse shaping by multilayer mirrors," Appl. Sci. **8**(12), 2503 (2018).
22. K. Ratra, M. Singh, A. K. Goyal, and R. Kaushik, "Design and analysis of broadband reflector for passive radiative cooling," *International Conference on Signal Processing and Communication (ICSC)* pp. 300–303 (2019).
23. M. Zahir and M. Benlattar, "A design of radiative cooler based on porous TiO_2 for improving solar cells performances," Appl. Opt. **60**(2), 445–451 (2021).

24. A. Kong, B. Cai, P. Shi, and X. cong Yuan, "Ultra-broadband all-dielectric metamaterial thermal emitter for passive radiative cooling," Opt. Express **27**(21), 30102–30115 (2019).

25. N. Jiménez, V. Romero-García, A. Cebrecos, R. Picó, V. Sánchez-Morcillo, and L. M. García-Raffi, "Broadband quasi perfect absorption using chirped multi-layer porous materials," AIP Adv. **6**(12), 121605 (2016).

26. H. V. Baghdasaryan, T. M. Knyazyan, T. T. Hovhannisyan, M. Marciniak, and L. Pajewski, "Enhancement of air-ground matching by means of a chirped multilayer structure: Electromagnetic modeling with the method of single expression," J. Telecommun. Inform.technology **3**(2017), 30–36 (2017).

27. M. De Carli and M. Tonon, "Effect of modelling solar radiation on the cooling performance of radiant floors," Sol. Energy **85**(5), 689–712 (2011).

28. M. Cho, J.-H. Seo, D. Zhao, J. Lee, K. Xiong, X. Yin, Y. Liu, S.-C. Liu, M. Kim, T. J. Kim, X. Wang, W. Zhou, and Z. Ma, "Amorphous Si/SiO$_2$ distributed Bragg reflectors with transfer printed single-crystalline Si nanomembranes," J. Vac. Sci. Technol., B: Nanotechnol. Microelectron.: Mater., Process., Meas., Phenom. **34**(4), 040601 (2016).

29. M. Neviere, *Light Propagation in Periodic Media: Differential Theory and Design (1st ed.)* (CRC Press, 1999), chap. Rigorous Coupled-Wave (RCW) Method.

30. K. C. Johnson, "Grating diffraction calculator," doi(2019) https://doi.org/10.24433/CO.7479617.v3.

31. M. Zeyghami, D. Y. Goswami, and E. Stefanakos, "A review of clear sky radiative cooling developments and applications in renewable power systems and passive building cooling," Sol. Energy Mater. Sol. Cells **178**, 115–128 (2018).

32. Z. Zhuang, Y. Xu, Q. Wu, B. Liu, B. Li, J. Zhao, and X. Yang, "Experimental study on the performance of a space radiation cooling system under different environmental factors," Energies **15**(19), 7404 (2022).

33. P. H. Tania Jorajuría, C. Lezáun, and M. Beruete, "Optimización de la emisividad teorica de un cuerpo para enfriamiento radiativo pasivo segun condiciones de temperatura," in *URSI 2021 Vigo XXXVI, Simposium Nacional de la Unión Científica Internacional de Radio* (Vigo, Spain, September 2021),.

34. C. Lezaun, J. S. Dolado, J. M. Pérez-Escudero, Í. Liberal, M. Beruete, and P. Herrera, "Análisis de los principales compuestos del cemento para enfriado radiativo, MIRACLE (project id: 964450)," (2021).

35. C. Zou, G. Ren, M. M. Hossain, S. Nirantar, W. Withayachumnankul, T. Ahmed, M. Bhaskaran, S. Sriram, M. Gu, and C. Fumeaux, "Metal-loaded dielectric resonator metasurfaces for radiative cooling," Adv. Opt. Mater. **5**(20), 1700460 (2017).

36. M. A. Kecebas, M. P. Menguc, A. Kosar, and K. Sendur, "Passive radiative cooling design with broadband optical thin-film filters," J. Quant. Spectrosc. Radiat. Transfer **198**, 179–186 (2017).

37. A. R. Gentle and G. B. Smith, "A subambient open roof surface under the mid-summer sun," Adv. Sci. **2**(9), 1500119 (2015).

38. J. Clark and K. Cahoy, "Optical detection of lasers with near-term technology at interstellar distances," The Astrophys. J. **867**(2), 97 (2018).

39. D. Galuzzo, C. Cagnazzo, F. Berrilli, F. Fierli, and L. Giovannelli, "Three-dimensional climate simulations for the detectability of proxima centauri b," The Astrophys. J. **909**(2), 191 (2021).

40. I. Ribas, E. Bolmont, F. Selsis, A. Reiners, J. Leconte, S. N. Raymond, S. G. Engle, E. F. Guinan, J. Morin, M. Turbet, F. Forget, and G. Anglada-Escudé, "The habitability of proxima centauri b - I. irradiation, rotation and volatile inventory from formation to the present," Astron. Astrophys. **596**, A111 (2016).